

COMPARISON OF TWO MODERATELY THICK PLATE ELEMENTS BASED ON THE ABSOLUTE NODAL COORDINATE FORMULATION

Marko K. Matikainen*, A. L. Schwab[†] and Aki M. Mikkola*

*Department of Mechanical Engineering
Lappeenranta University of Technology, Skinnarilankatu 34, FI-53850 Lappeenranta, Finland
e-mails: marko.matikainen@lut.fi, aki.mikkola@lut.fi

[†]Laboratory for Engineering Mechanics
Delft University of Technology, Mekelweg 2, NL-2628 CD Delft, The Netherlands
e-mails: a.l.schwab@tudelft.nl

Keywords: plate elements, flexible multibody dynamics, benchmark problems.

Abstract. *Two formulations for a flexible 3-D quadrilateral moderately thick plate element based on the absolute nodal coordinate formulation are compared. The two approaches consist of a fully parameterized plate element and a fully parameterized plate element with linearized transverse shear angles to overcome slow convergence and curvature locking. For the sake of verification of the formulations and numerical tests, a thin plate element based on a classical Discrete Kirchhoff Triangle in large displacement framework is also utilized. A comparison is accomplished through use of the comprehensive set of small deformation static tests and eigenfrequency analyses. These results are benchmarked to known analytical solutions.*

It is shown that plate elements based on absolute nodal coordinate formulation reach the same result and convergence for pure bending loads. However, under shear deformation loading, slow convergence due to shear locking occurs in the case of an original plate element. The numerical examples indicate that thickness locking (known also as Poisson locking) is a problem for both of the plate elements based on absolute nodal coordinate formulation. Thickness locking arises when full 3-D elasticity is employed in the fully parameterized elements. All computations are implemented using MATLAB.

1 INTRODUCTION

The nonlinear continuum plate/shell elements have been under active research for more than four decades. Usually, these conventional continuum plate/shell elements utilize rotation parameters instead of slope vectors. It has been previously introduced that continuum shell elements, with fully three-dimensional stresses and strains, can be degenerated to shell element behavior such that the kinematics and constitutive assumptions of shells are acceptable, see for example [1]. This isoparametric continuum shell element (known as A-I-Z shell element) is based on the Mindlin/Reissner hypothesis. The element includes 3 translational and 2 rotational parameters at a node. However, it is known that the A-I-Z shell element suffers from shear locking, which can be alleviated with the introduction of separate linear interpolations for transverse shear deformations in a four node shell element (known as MITCH4 shell element) [2]. The original MITCH4 element is derived from the A-I-Z shell element using the same five node parameters, the only difference is that shear locking is avoided by using mixed interpolation. To be able to use general 3-D elasticity without making any modifications due to degeneration such as condensation of thickness strain is worth the addition of thickness deformation in the continuum shell formulation. Additionally, in case of large strains, the thickness deformation has to be taken into account. However, the interpolation for displacement in the thickness direction must be larger than linear, otherwise, with fully 3-D elasticity it is a source of thickness locking. Due to this fact, the 7-parameter formulation is introduced [3] which means there will be two extra parameters at a node, allowing for linear stretching in the thickness direction. Also, the shell element based on MITCH4 formulation, which uses only 22 degrees of freedom including five generalized displacements at node and two for linear thickness stretching, has been introduced in [4]

The absolute nodal coordinate formulation (ANCF) is a finite element procedure that was recently proposed for flexible multibody applications by Shabana [5]. The formulation can be applied to conventional as well as shear deformable beam and plate elements. In the shear deformable elements, the beam and plate elements can be described as continuum by using the positions and position gradients as nodal coordinates. In contrast to conventional beam and plate elements, position gradients of the material point within the element are derivatives of the displacement field. In continuum beam and plate/shell elements, the kinematics and constitutive assumptions for conventional beam and plates/shell theories can be relaxed. Because of the material description, the strain and stress quantities are frame-indifferent, leading to the possibility to describe large deformation problems. This can be accomplished, for example, by using a nonlinear material model based on hyperelasticity [6, 7]. In the absolute nodal coordinate formulation, the description of the material point is described through use of shape functions and nodal coordinates. It is worth noting that this description accounts for large rigid body rotations of the finite elements. This leads to a constant mass matrix in two and three dimensional applications and is a unique feature among the beam and plate elements based on the absolute nodal coordinate formulation [8].

The first ANCF plate element was developed by Shabana and Christensen [9]. This plate element was based on the classical (Kirchoff-Love) plate theory while rotation parameters were used only to describe the bending deformation. In order to account for the shear deformation and thickness deformation, in case of thick plates, the fully parameterized quadrilateral plate element was developed [10]. Full-parameterization indicates usage of the position vector and all position vector gradients as variables at nodal locations. Another fully parameterized quadrilateral plate element was introduced to overcome the slow convergence due to shear locking

and curvature locking [11]. It is noteworthy that the fully parameterized plate elements under investigation are based on an identical approximation for in-plane, the only difference being the description for kinematics in the transversal direction. These fully parameterized plate elements are based on continuum mechanics theory and fully three-dimensional strain and stress tensors are employed in the formulations. As a result, these continuum elements should be applicable for the analyses of thin and thick plates and any general material law based on continuum mechanics can be used. The main difference between conventional finite elements and ANCF elements is that the mass matrix is constant for ANCF elements. This is computationally efficient if explicit integrators are used. Additionally, there are no geometrical approximations included in the ANCF elements [12], which is seldom the case for conventional structural finite elements.

The purpose of this study is to make comparisons between two moderately thick plate elements based on the absolute nodal coordinate formulation. These fully parameterized plate elements are employed in simple numerical examples in which advantages and disadvantages of the elements can be demonstrated. Verification of the two elements is accomplished through numerical examples in framework of thin and thick plates. In this study, the elastic forces of fully parameterized elements are made by using full Gaussian integration to show that the elements are performing properly.

2 KINEMATICS OF FULLY-PARAMETERIZED PLATE ELEMENT

In this section, the fully parameterized plate element by Mikkola and Shabana [10] will be shortly revisited. This four-node quadrilateral plate element, which is denoted in this study as ANCF-P48, consists of 48 degrees of freedom. Three degrees of freedom are for position and nine are for gradients at each node. In elements based on the absolute nodal coordinate formulation, kinematics is expressed by using spatial shape functions and global coordinates, similar to conventional solid elements. The position of an arbitrary particle in the isoparametric fully parameterized plate element can be interpolated in the global fixed frame as follows:

$$\mathbf{r} = \mathbf{S}_m(\mathbf{x})\mathbf{e}, \quad (1)$$

where \mathbf{S}_m is a shape function matrix expressed using physical element coordinates \mathbf{x} and $\mathbf{e} = \mathbf{e}(t)$ is the vector of nodal coordinates. The kinematics of the element on the reference configuration at time $t = 0$ can be described as $\mathbf{r}_0 = \mathbf{S}_m(\mathbf{x})\mathbf{e}_0$, where $\mathbf{e}_0 = \mathbf{e}(0)$. In Fig. 1, the fully parameterized undeformed plate element at current configuration with dimensions of width l_x , length l_y and thickness l_z are shown.

The vector of nodal coordinates at node i can be written as follows:

$$\mathbf{e}^{(i)} = \left[\mathbf{r}^{(i)T} \quad \mathbf{r}_{,x}^{(i)T} \quad \mathbf{r}_{,y}^{(i)T} \quad \mathbf{r}_{,z}^{(i)T} \right]^T; \quad i = 1, \dots, 4 \quad (2)$$

where \mathbf{r} is the position vector of the element and x , y and z are physical coordinates of the element. In this study, the following notation for partial derivatives is used:

$$\mathbf{r}_{,\alpha}^{(i)} = \begin{bmatrix} r_{1,\alpha}^{(i)} \\ r_{2,\alpha}^{(i)} \\ r_{3,\alpha}^{(i)} \end{bmatrix} = \frac{\partial \mathbf{r}^{(i)}}{\partial \alpha}; \quad \alpha = x, y, z.$$

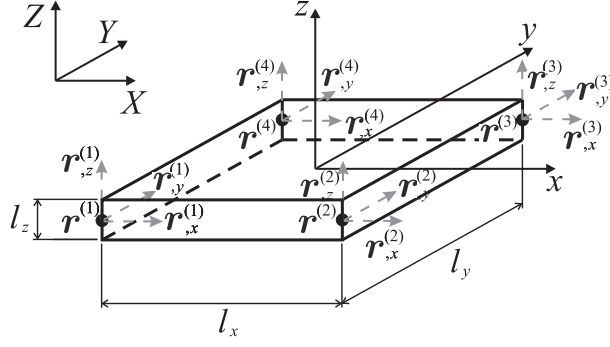


Figure 1: Undeformed plate element with its dimensions in current configuration.

The interpolation functions for position are based on the following set of basis polynomials

$$[1, x, y, z, xz, yz, yx, x^2, y^2, x^3, y^3, x^2y, y^2x, xyz, x^3y, xy^3] \quad (3)$$

Note that the basis polynomials in Eq. (3) are incomplete, and for this reason, the element has linear terms only in transverse coordinate z . Accordingly, the displacement distribution is linear in the element's transverse direction. The interpolation for position is cubic in the in-plane coordinates x and y . The shape functions can be presented through use of local normalized coordinates, such as $\xi, \eta, \zeta \in [-1 \dots 1]$, and are listed below:

$$\begin{aligned} S_1 &= \frac{(-1+\xi)(1-\eta)(\xi^2+\xi+\eta^2+\eta-2)}{8}, & S_2 &= \frac{l_x(1-\eta)(1+\xi)(-1+\xi)^2}{16}, \\ S_3 &= \frac{l_y(1-\xi)(\eta+1)(-1+\eta)^2}{16}, & S_4 &= \frac{l_z\zeta(-1+\xi)(-1+\eta)}{8}, \\ S_5 &= \frac{(1+\xi)(-1+\eta)(\xi^2-\xi+\eta^2+\eta-2)}{8}, & S_6 &= \frac{l_x(1-\xi)(-1+\eta)(1+\xi)^2}{16}, \\ S_7 &= \frac{l_y(1+\xi)(\eta+1)(-1+\eta)^2}{16}, & S_8 &= \frac{l_z\zeta(1+\xi)(1-\eta)}{8}, \\ S_9 &= \frac{(1+\xi)(-\eta-1)(\xi^2-\xi+\eta^2-\eta-2)}{8}, & S_{10} &= \frac{l_x(-1+\xi)(\eta+1)(1+\xi)^2}{16}, \\ S_{11} &= \frac{l_y(1+\xi)(-1+\eta)(\eta+1)^2}{16}, & S_{12} &= \frac{l_z\zeta(1+\xi)(\eta+1)}{8}, \\ S_{13} &= \frac{(-1+\xi)(\eta+1)(\xi^2+\xi+\eta^2-\eta-2)}{8}, & S_{14} &= \frac{l_x(1+\xi)(\eta+1)(-1+\xi)^2}{16}, \\ S_{15} &= \frac{l_y(-1+\xi)(1-\eta)(\eta+1)^2}{16}, & S_{16} &= \frac{l_z\zeta(\eta+1)(1-\xi)}{8} \end{aligned} \quad (4)$$

where relations $\xi = 2x/l_x$, $\eta = 2y/l_y$ and $\zeta = 2z/l_z$ when the physical coordinate system x, y, z is placed along the middle of the element. These shape-functions can be represented in matrix form as:

$$\mathbf{S}_m = [S_1 \mathbf{I} \quad S_2 \mathbf{I} \quad S_3 \mathbf{I} \quad \dots \quad S_{16} \mathbf{I}] \quad (5)$$

where \mathbf{I} is a 3×3 identity matrix. Due to the isoparametric property of the element, the kinematics (1) can also be expressed in terms of local normalized coordinates $\mathbf{r} = \mathbf{S}_m(\xi, \eta, \zeta)\mathbf{e}$.

The strains can be obtained by using the Green strain tensor \mathbf{E} which can be written for the plate element as

$$\mathbf{E} = \frac{1}{2}(\nabla \mathbf{r}^T \nabla \mathbf{r} - \mathbf{I}), \quad (6)$$

where $\nabla \mathbf{r}$ is the deformation gradient. The deformation gradient can be shown through the relationship of deformations between the initial $\mathbf{r}_0 = \mathbf{S}_m \mathbf{e}(t=0) = \mathbf{S}_m \mathbf{e}_0$ and current configuration \mathbf{r} as follows:

$$\nabla \mathbf{r} = \frac{\partial \mathbf{r}}{\partial \mathbf{r}_0} = \frac{\partial \mathbf{r}}{\partial \mathbf{x}} \left(\frac{\partial \mathbf{r}_0}{\partial \mathbf{x}} \right)^{-1}. \quad (7)$$

Using the engineering notations, the strains can be written in vector form as

$$\boldsymbol{\varepsilon} = [E_{xx} \quad E_{yy} \quad E_{zz} \quad 2E_{yz} \quad 2E_{xz} \quad 2E_{xy}]^T \quad (8)$$

3 KINEMATICS OF PLATE ELEMENT WITH LINEARIZED SHEAR ANGLES

The plate element with linearized shear angles [11], denoted in this study as ANCF-P48lsa, leads to an improved definition of the elastic forces, since the use of linearized shear angles overcomes the shear locking and curvature locking associated with the plate element. The plate element with linearized shear angles is based on the same in-plane interpolation functions as the original fully parameterized plate element [10]. When compared to the original element ANCF-P48, however, the fiber deformation of the plate element ANCF-P48lsa is modified in order to linearize the transverse shear deformations. This approach for avoid shear locking is well known among classical MITCH shell elements [2]. The same effect can also be avoided by the Hellinger-Reissner variational principle, which has been applied to the ANCF beam element in [13]. Slow convergence due to shear locking can also be improved by using additional shape function terms, which are employed in higher order beam elements based on the absolute nodal coordinate formulation [14]. In plate element ANCF-P48lsa, the description of an arbitrary particle in the element can be expressed as

$$\mathbf{r}_e = \mathbf{r} \Big|_{z=0} + \mathbf{A}_{1s} \mathbf{A}_{2s} \hat{\mathbf{n}} z. \quad (9)$$

The vector $\hat{\mathbf{n}}$ describes the unit transverse vector of the mid-plane, which can be expressed with the aid of slope vectors as follows:

$$\hat{\mathbf{n}} = \frac{\mathbf{r}_{,x} \times \mathbf{r}_{,y}}{\|\mathbf{r}_{,x} \times \mathbf{r}_{,y}\|} \Big|_{z=0}, \quad (10)$$

The vector $\hat{\mathbf{n}}$ is normal to mid-plane and, therefore, it is invariant with respect to transverse shear deformation. The normalization leads to a cumbersome equation, but it is worth noting that the error due to shrinking will be avoided simultaneously. The matrices \mathbf{A}_{1s} and \mathbf{A}_{2s} are used to describe the transverse shear deformation. These matrices can be obtained by using the Rodrigues rotation formula and by assuming that the shear angles are small as follows:

$$\mathbf{A}_{1s} = \mathbf{I} + \tilde{\mathbf{r}}_{,x} \sin \gamma_1 + 2 \tilde{\mathbf{r}}_{,x}^2 \sin^2 \frac{\gamma_1}{2} \approx \mathbf{I} + \tilde{\mathbf{r}}_{,x} \gamma_1, \quad (11a)$$

$$\mathbf{A}_{2s} = \mathbf{I} + \tilde{\mathbf{r}}_{,y} \sin \gamma_2 + 2 \tilde{\mathbf{r}}_{,y}^2 \sin^2 \frac{\gamma_2}{2} \approx \mathbf{I} + \tilde{\mathbf{r}}_{,y} \gamma_2 \quad (11b)$$

where γ_1 and γ_2 are the shear angles with respect to slopes $\mathbf{r}_{,x}$ and $\mathbf{r}_{,y}$ that define the direction of rotation. A skew-symmetric matrix $\tilde{\mathbf{r}}_{,x}$ is determined by the unit vector $\hat{\mathbf{r}}_{,x}$ and, respectively, a skew-symmetric matrix $\tilde{\mathbf{r}}_{,y}$ is determined by the unit vector $\hat{\mathbf{r}}_{,y}$. Utilizing the property of the

absolute nodal coordinate formulation, the shear angles γ_1 and γ_2 can be derived from the slope vectors as follows:

$$\sin \gamma_1 = \frac{\mathbf{r}_{,y}^T \mathbf{r}_{,z}}{\|\mathbf{r}_{,y}\| \|\mathbf{r}_{,z}\|} \approx \gamma_1 \quad \text{and} \quad \sin \gamma_2 = -\frac{\mathbf{r}_{,x}^T \mathbf{r}_{,z}}{\|\mathbf{r}_{,x}\| \|\mathbf{r}_{,z}\|} \approx \gamma_2. \quad (12)$$

In this case, shear angles in the element will be interpolated in-plane by fourth order polynomials. However, it is known that nonlinear interpolations for shear deformations can lead to slow convergence, which can be alleviated by linear interpolation for transverse shear deformations [2]. For plate element ANCF-P48lsa, a slightly different approach for the interpolation of shear deformation is employed. To guarantee that parasitic strain distribution is zero, the nodal values are used instead of sampling points [15]. Therefore, the bilinear interpolation for the shear angles are used i.e. the shear angles are interpolated linearly over the length and width of the element using the following equations:

$$\gamma_1^{\text{lin}} = \sum_{i=1}^4 N^{(i)} \gamma_1^{(i)} \quad \text{and} \quad \gamma_2^{\text{lin}} = \sum_{i=1}^4 N^{(i)} \gamma_2^{(i)} \quad (13)$$

where $N^{(i)}$ are bilinear shape functions at mid-plane. With the linearized Rodrigues rotation formula and the shear angles, the rotation matrices \mathbf{A}_{1s} and \mathbf{A}_{2s} take the form:

$$\mathbf{A}_{1s} \approx \mathbf{I} + \tilde{\mathbf{r}}_{,x} \gamma_1^{\text{lin}} \quad \text{and} \quad \mathbf{A}_{2s} \approx \mathbf{I} + \tilde{\mathbf{r}}_{,y} \gamma_2^{\text{lin}}. \quad (14)$$

According to [11], in case of small displacements and when elements at current configuration are in axis-parallel to reference configuration, unit vectors can be expressed by $\tilde{\mathbf{r}}_{,x} = [1 \ 0 \ 0]^T$ and $\tilde{\mathbf{r}}_{,y} = [0 \ 1 \ 0]^T$. Using this simplification, the product of shear matrices can be expressed as follows:

$$\mathbf{A}_{1s} \mathbf{A}_{2s} \approx \begin{pmatrix} 1 & 0 & \gamma_2^{\text{lin}} \\ 0 & 1 & -\gamma_1^{\text{lin}} \\ -\gamma_2^{\text{lin}} & \gamma_1^{\text{lin}} & 1 \end{pmatrix}, \quad (15)$$

where quadratic term $\gamma_1^{\text{lin}} \gamma_2^{\text{lin}}$ is neglected. The strains can be obtained by using the Green strain (6). As a result, the strain components can be expressed as:

$$\begin{aligned} E_{xx} &= \frac{1}{2} (\mathbf{r}_{e,x}^T \mathbf{r}_{e,x} - 1), & E_{yy} &= \frac{1}{2} (\mathbf{r}_{e,y}^T \mathbf{r}_{e,y} - 1), \\ E_{xy} &= \frac{1}{2} (\mathbf{r}_{e,x}^T \mathbf{r}_{e,y}), & E_{xz} &= \frac{1}{2} (\mathbf{r}_{e,x}^T \mathbf{r}_{e,z}), & E_{yz} &= \frac{1}{2} (\mathbf{r}_{e,y}^T \mathbf{r}_{e,z}). \end{aligned} \quad (16)$$

The strain component E_{zz} in the element thickness direction can not be defined with kinematics, as described by \mathbf{r}_e (9). The strain component E_{zz} can be obtained from kinematics \mathbf{r} of the fully parameterized plate element (1) as follows:

$$E_{zz} = \frac{1}{2} (\mathbf{r}_{,z}^T \mathbf{r}_{,z} - 1). \quad (17)$$

The strain component E_{zz} can also be interpolated with the use of bilinear shape functions, which can be used to avoid the curvature locking (also called trapezoidal locking), see for example [15, 16]. Therefore, the bilinear strain distribution E_{zz}^{lin} along the length and width

of the element is used in this study. The strain components can be shown in vector form $\boldsymbol{\varepsilon}$ as follows:

$$\boldsymbol{\varepsilon} = \left[E_{xx} \quad E_{yy} \quad E_{zz}^{\text{lin}} \quad 2E_{xy} \quad 2E_{xz} \quad 2E_{yz} \right]^T \quad (18)$$

where kinematics with linearized shear angles is used for all strain components except E_{zz}^{lin} .

4 ELASTIC FORCES, EXTERNAL FORCES AND MASS MATRIX

In the ANCF elements, the general hyperelastic materials can be used in the definition of the elastic forces. However, in this work, 3-D elasticity for the fully parameterized plate elements is described by using the simple linear elastic St. Venant-Kirchhoff material, which is valid in small strain regime. The constitutive relation in case of linear elastic St. Venant-Kirchhoff material can be expressed as

$$\boldsymbol{S} = {}^4\boldsymbol{D} : \boldsymbol{E} \quad (19)$$

where the fourth order tensor ${}^4\boldsymbol{D}$ includes the properties of the material. In case of an elastic isotropic material, the relation between the second Piola-Kirchhoff stress tensor and the Green strain tensor takes the form

$$\boldsymbol{S} = \lambda \text{Tr}(\boldsymbol{E}) + 2G\boldsymbol{E}, \quad (20)$$

where λ and G are the Lamé elastic constants. The strain energy of one plate element can be written as

$$W_{\text{int}} = \frac{1}{2} \int_V \boldsymbol{\varepsilon}^T \boldsymbol{D} \boldsymbol{\varepsilon} \, dV \quad (21)$$

and the vector of elastic forces can be defined as

$$\boldsymbol{F}_e = \frac{\partial W_{\text{int}}}{\partial \boldsymbol{e}}^T. \quad (22)$$

The externally applied forces can be determined from

$$\boldsymbol{F}_{\text{ext}} = \int_V \boldsymbol{b}^T \boldsymbol{S}_m \, dV. \quad (23)$$

where \boldsymbol{b} is the vector of body forces. In the special case of gravity, the body forces can be written as $\boldsymbol{b} = \rho \boldsymbol{g}$ where \boldsymbol{g} is the field of gravity. Using the definition for kinematics of the fully parameterized plate element (1), the absolute nodal coordinate formulation leads to a constant mass matrix as follows:

$$\boldsymbol{M} = \int_V \rho \boldsymbol{S}_m^T \boldsymbol{S}_m \, dV. \quad (24)$$

In case of a linearized shear angle, the mass matrix would no longer be constant if the same interpolation, as for the elastic forces, is used (9). However, this error is due to inconsistencies between kinematics and kinetic energy and will decrease in value with the use of finer meshes.

5 NUMERICAL TESTS FOR THIN PLATE

The two plate elements presented in this study account for the transverse shear deformation and nonlinear strain-displacement relationship. For this reason, elements are not restricted to thin plate and small displacement, although the first numerical verification is carried out in this regime. The convergence is studied by mesh refinement for static and eigenvalue tests. The numerical tests, such as the cantilever plate and eigenfrequency analyses, used in this study are originally introduced by Schwab et. al [17] for verification of thin ANCF plate. The regular meshes $n \times n$, as shown in Fig. 2, are used.

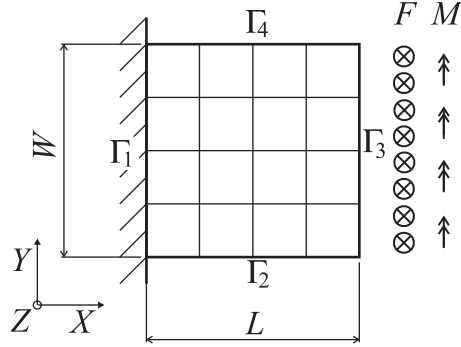


Figure 2: Loading, boundaries and uniform 4×4 mesh of a square cantilevered plate with quadrilateral elements.

5.1 CANTILEVER PLATE

The first numerical test is a linear static analysis of an infinitely-wide cantilever plate under two different loading conditions. The first loading case is a distributed moment and the second is a distributed transverse force along the free edge of the structure. The numerical solutions are compared to the analytical exact solutions for transverse displacement, which in the case of static analysis are found to be as follows:

$$w_{exact} = \frac{ML^2}{2D} + \frac{FL^2}{3D} \quad \text{and} \quad \varphi_{exact} = \frac{ML}{D} + \frac{FL^2}{2D} \quad (25)$$

where M is distributed moment, F is distributed force along the loaded edge and D is the elastic plate constant defined as follows $D = EH^2/(12(1 - \nu^2))$. The results of the computations for the transverse displacement w and rotation along the loaded edge about y -axis φ are normalized with respect to exact analytical results. The rotation angle φ which defines the rotation due to shear and bending for ANCF plate elements, can be expressed as follows:

$$\varphi = \arccos \frac{\mathbf{r}_{0,z}^T \mathbf{r}_{,z}}{\|\mathbf{r}_{0,z}\| \|\mathbf{r}_{,z}\|} \quad (26)$$

where \mathbf{r}_0 is defined such that \mathbf{e}_0 is vector of nodal coordinates at the initial configuration. In this example, $\mathbf{r}_{0,z} = [0, 0, 1]^T$ is the transverse slope at the initial undeformed configuration. The test is modeled with the following parameters: length $L = 1$ m, height $H = 0.01$ m, width $W = 1$ m, Young's modulus $E = 210 \cdot 10^9 \frac{\text{N}}{\text{m}^2}$, shear modulus $G = \frac{E}{2(1+\nu)}$, shear correction factor $k_s = 1$, Poisson's ratio $\nu = 0.3$, the distributed moment $M = 1$ Nm/m and force $F = 1$ N/m. At the clamped end, the boundary condition is defined by fixing all the nodal degrees of freedom at Γ_1 . In reference [17], the component $r_{2,y}$ was unfixed in the clamped

boundary to allow the in-plane deformation. However, in this study, the slow convergence due to the fixed component $r_{2,y}$ was not observed. The analytical solutions are defined for a cantilever plate with infinite width W . For this reason, the in-plane component $r_{3,y}$ is fixed in order to avoid in-plane rotation along the boundaries Γ_2 and Γ_4 . However, transverse shear deformation γ_{yz} is still unconstrained in order to avoid slow convergence. The boundary Γ_3 is unconstrained while it is loaded by the distributed force F or moment M .

Table 1: Average normalized transverse displacements \bar{w} and rotations $\bar{\varphi}$ at the loaded edge for a square cantilevered plate loaded by a distributed moment or a distributed transverse force at the free edge for number of mesh refinements and two different element types with $\nu=0.3$.

Mesh	Moment		Transverse force	
	ANCF-P48	ANCF-P48lsa	ANCF-P48	ANCF-P48lsa
	\bar{w}	\bar{w}	\bar{w}	\bar{w}
1x1	0.8164	0.8164	0.6123	0.8164
2x2	0.8164	0.8164	0.7654	0.8164
4x4	0.8166	0.8164	0.8039	0.8165
8x8	0.8169	0.8165	0.8137	0.8166
16x16	0.8174	0.8168	0.8167	0.8168
32x32	0.8185	0.8172	0.8183	0.8173
64x64	0.8205	0.8181	0.8204	0.8182
	$\bar{\varphi}$	$\bar{\varphi}$	$\bar{\varphi}$	$\bar{\varphi}$
1x1	0.8164	0.8164	0.8164	0.8164
2x2	0.8165	0.8164	0.8165	0.8164
4x4	0.8167	0.8164	0.8166	0.8164
8x8	0.8170	0.8166	0.8169	0.8166
16x16	0.8175	0.8168	0.8174	0.8168
32x32	0.8186	0.8173	0.8185	0.8173
64x64	0.8207	0.8182	0.8206	0.8182

As can be seen from results in Table 1, the chosen boundary conditions lead to acceptable results, as errors are almost equal in both loading cases. In case of the transverse loading force, the convergence of ANCF-P48lsa is significantly faster than the original fully parameterized plate element. This is due to shear locking, which is avoided by linearization of transverse shear angles in ANCF-P48lsa. However, both elements converge to an incorrect solution under both loading cases. The reason for this is thickness locking, which is due to low order interpolation approximation in the element transverse direction in full 3-D elasticity. In case of spatial beam elements, locking can be avoided by neglecting Poisson effect with $\nu=0$, as explained in [18]. Correspondingly, in case of continuum plates and shells, different modified material laws can be used to overcome the thickness locking for thin plate/shells [19].

5.2 EIGENFREQUENCIES AND CHLADNI FIGURES

The second test is an eigenfrequency analysis with free boundaries. The eigenfrequencies ω are nondimensionalized by the frequency $\omega_0 = \pi^2 \sqrt{D/\rho H L^4}$ and the analytical results for eigenvalue analysis are obtained from reference [17]. The eigenmodes will be presented as Chladni figures, where lines of nodes without displacements are shown. Studies of the thin plate SPACAR element and the fully parameterized plate element ANCF-P48 are also presented

in [17]. In this numerical example, a relative plate thickness of $H/L = 0.01$ was used. The eigenfrequencies for the case of free boundary conditions are expressed in Tables 2-3 where in-plane modes denoted by – are not shown.

Table 2: First ten dimensionless eigenfrequencies $\Omega = \omega/\omega_0$ of the free transverse free (ffff) square plate modeled by the ANCF-P48 with Poisson factor $\nu = 0.3$ for a number of mesh refinements. A relative plate thickness of $H/L = 0.01$ was used.

No.	1x1	2x2	4x4	8x8	16x16	32x32	64x64	Analytic
1	1.4383	1.4381	1.4245	1.3870	1.3739	1.3715	1.3701	1.3646
2	2.2739	2.2738	2.0761	2.0396	2.0268	2.0241	2.0235	1.9855
3	3.5947	3.5944	2.9253	2.8184	2.7867	2.7798	2.7781	2.4591
4	71.994	7.9946	5.5712	3.8034	3.6448	3.6284	3.6234	3.5261
5	71.994	7.9946	5.5712	3.8034	3.6448	3.6284	3.6234	3.5261
6	–	18.036	7.8878	7.0253	6.8120	6.7653	6.6851	6.1900
7	–	18.036	7.8878	7.0253	6.8120	6.7653	6.7541	6.1900
8	–	54.593	14.9194	7.4395	6.7585	6.6985	6.7541	6.4528
9	–	72.227	16.687	7.9823	7.2925	7.2245	7.2095	7.0181
10	–	72.524	17.665	9.3391	8.6230	8.5354	8.5162	7.8191

Table 3: First ten dimensionless eigenfrequencies $\Omega = \omega/\omega_0$ of the free transverse free (ffff) square plate modeled by the ANCF-P48lsa with Poisson factor $\nu = 0.3$ for a number of mesh refinements. A relative plate thickness of $H/L = 0.01$ was used.

No.	1x1	2x2	4x4	8x8	16x16	32x32	64x64	Analytic
1	1.3999	1.3918	1.3797	1.3747	1.3727	1.3714	1.3701	1.3646
2	2.2739	2.0307	2.0340	2.0268	2.0243	2.0236	2.0234	1.9855
3	3.5948	2.7949	2.8104	2.7875	2.7805	2.7785	2.7778	2.4591
4	4.1709	3.5484	3.6349	3.6335	3.6296	3.6266	3.6231	3.5261
5	4.1709	3.5484	3.6349	3.6335	3.6296	3.6266	3.6231	3.5261
6	10.328	7.7428	6.8913	6.7999	6.7651	6.7550	6.6834	6.1900
7	10.328	7.7428	6.8913	6.7999	6.7651	6.7545	6.7516	6.1900
8	–	6.6779	6.5930	6.6671	6.6888	6.6898	6.7516	6.4528
9	9.1662	7.8723	7.3146	7.2603	7.2289	7.2163	7.2079	7.0181
10	13.517	9.7664	8.4230	8.5262	8.5237	8.5178	8.5123	7.8191

As can be seen from the tables, the convergence of ANCF-P48lsa is considerably faster than in the case of ANCF-P48. In order to emphasize the difference between plate elements ANCF-P48 and ANCF-P48lsa, the convergence of the first mode (see top left mode in Fig. 4) is also considered for thin plates, in which the relative plate thickness is assumed to be $H/L = 0.001$. Fig. 3 shows that ANCF-P48lsa is not sensitive in terms of the convergence of the first mode of the thin plate. Accordingly, in the case of a thin plate, the convergence of the first mode does not depend on a relative plate thickness of H/L , as such is the case for ANCF-P48. This type of locking phenomenon is known as shear locking. It seems that the first bending mode includes shear deformation, resulting in the slow convergence of ANCF-P48. However both plate elements are again converged to the same incorrect result, due to thickness locking. In this

numerical example, two different relative plate thicknesses of $H/L = 0.01$ and $H/L = 0.001$ were used. The eigenmodes for the plate element ANCF-P48l1sa are illustrated by using Chladni figures (lines of nodes) in Fig. 4, which agrees with earlier reported Chladni figures based on SPACAR thin elements [17].

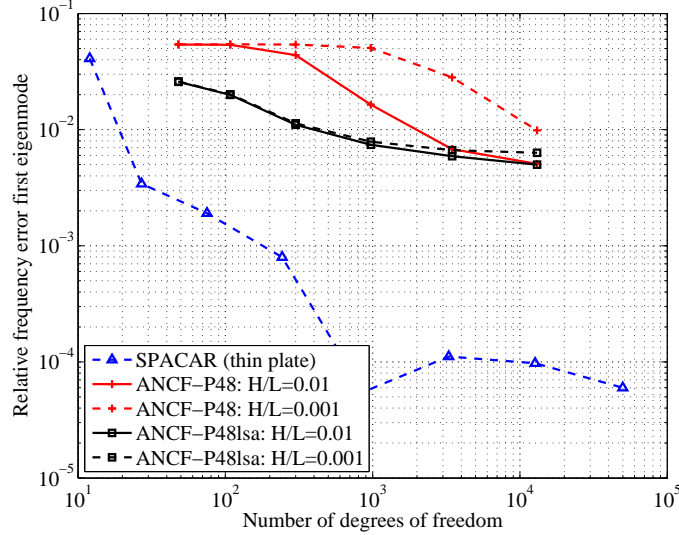


Figure 3: Convergences of the first mode normalized by analytical solution for free (ffff) square plate as calculated by the SPACAR, ANCF-P48 and ANCF-P48l1sa with Poisson factor $\nu=0.3$. Two different relative plate thickness of $H/L=0.01$ and $H/L=0.001$ were used.

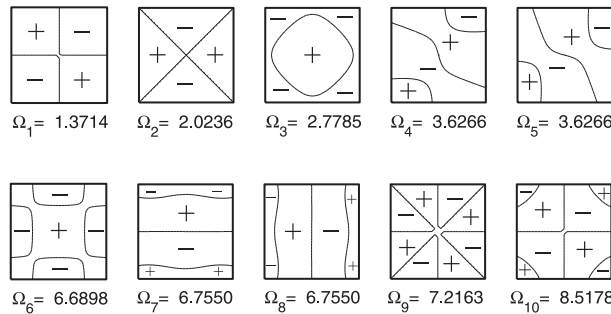


Figure 4: First 10 transverse vibration modes together with their dimensionless frequencies for free (ffff) square plate as calculated by the ANCF-P48l1sa with a mesh 32×32 and Poisson factor $\nu=0.3$. A relative plate thickness of $H/L = 0.01$ was used.

In [17], in-plane modes of ANCF-P48 are discussed. It is important to note that in-plane modes of ANCF-P48 and ANCF-P48l1sa are identical and, therefore, in-plane modes are not depicted.

5.3 PURE BENDING TEST

In this section, introduced plate elements based on the absolute nodal coordinate formulation are employed in a pure bending study. Figure 5 (a) illustrates a particular case of pure bending which may be obtained by using distributed twisting moments M applied on the free edges of

the plate. According to [20], an identical displacement field can be created from the moments M for the portion $abcd$ (Fig. 5 (a)) or by applying nodal forces $2ML$ at corners a, b, c and d (Fig. 5 (b)). In the latter loading case, the in-plane shear is constant if the normal vector has unit length [21]. Therefore, it can be assumed that in-plane shear locking is not dominating in this loading case. These examples are solved by using three different plate elements: SPACAR three node thin plate element (18 dofs), ANCF-P48 and ANCF-P48lsa.

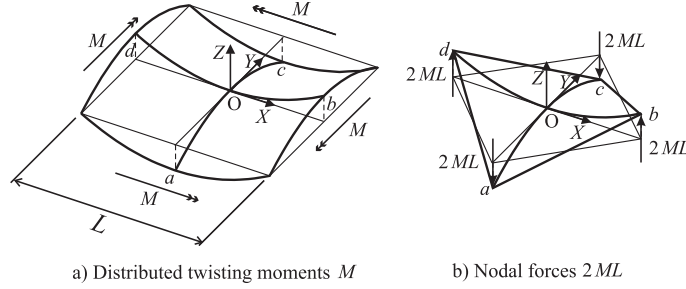


Figure 5: Particular cases of pure bending caused by distributed twisting moment M and nodal forces $2ML$.

The boundary conditions for the SPACAR element are relatively straightforward to define: all degrees of freedom at origin node O are fixed. In case of ANCF-plates, the boundary conditions are as follows: all degrees of freedom at node O are fixed except for $r_{1,x}, r_{2,y}$ and $r_{3,z}$. The meshes for the different loading cases are shown in Fig. 6.

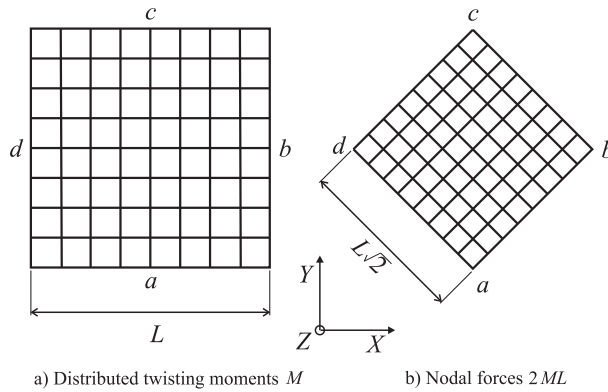


Figure 6: Square meshes 8×8 for different loading cases.

Displacement at the asymptotic line for moderately thick plates is considered in this numerical example. In the case of small deflections and moderately thick plates, deflection w in direction Z can be defined for an anticlastic surface [20] as follows

$$w = \frac{M}{2D(1-\nu)}(X^2 - Y^2) \quad (27)$$

where $D = EH^3/(12(1-\nu^2))$. The rotation at point a about the X -axis can be defined as

$$\varphi = \frac{M}{D(1-\nu)}Y \quad (28)$$

The parameters used in the plate example are as follows: length $L = 1$ m, Young's modulus $E = 210 \cdot 10^9 \frac{\text{N}}{\text{m}^2}$, shear modulus $G = \frac{E}{2(1+\nu)}$, shear correction factor $k_s = 1$, Poisson's ratio $\nu = 0.3$ and the distributed moment $M = 1\text{Nm/m}$. The computed displacements and rotations for elements SPACAR, ANCF-P48 and ANCF-P48lsa ($H/L = 0.01$ for thin plates and $H/L = 0.2$ for thick plates, shown in Table 4) are normalized by the analytical solution from Eq. (27) and the analytical solution from Eq. (28).

Table 4: Normalized displacement at point a (Figure 5) of the square thin plate modeled by SPACAR, ANCF-P48 and ANCF-P48lsa elements. A relative plate thickness of $H/L = 0.01$ was used.

Mesh	SPACAR		ANCF-P48		ANCF-P48lsa	
	Moment	Forces	Moment	Forces	Moment	Forces
	\bar{w}	\bar{w}	\bar{w}	\bar{w}	\bar{w}	\bar{w}
2x2	1.014122	1.027241	1.000000	1.001077	1.000000	1.000400
4x4	1.003721	1.012120	1.000000	1.001692	1.000000	1.000914
8x8	1.000873	1.005163	1.000000	1.002260	1.000000	1.001839
16x16	1.000210	1.002256	1.000000	1.003832	1.000000	1.003622
32x32	1.000052	1.001033	1.000000	1.006936	1.000000	1.006809
64x64	1.000013	1.000491	1.000000	1.011303	1.000000	1.011196

Table 5: Normalized rotations $\bar{\varphi}$ and shear angles $\bar{\gamma}$ at point a (Figure 5) of the square thin plate modeled by SPACAR, ANCF-P48 and ANCF-P48lsa elements. A relative plate thickness of $H/L = 0.01$ was used.

Mesh	SPACAR		ANCF-P48		ANCF-P48lsa	
	Moment	Forces	Moment	Forces	Moment	Forces
	$\bar{\varphi}$	$\bar{\varphi}$	$\bar{\varphi}$	$\bar{\varphi}$	$\bar{\varphi}$	$\bar{\varphi}$
2x2	1.024127	1.050475	1.000000	1.002648	1.000000	1.000000
4x4	1.007862	1.025814	1.000000	1.010236	1.000000	1.000268
8x8	1.003778	1.013677	1.000000	1.009877	1.000000	1.001040
16x16	1.001864	1.007268	1.000000	1.009454	1.000000	1.003054
32x32	1.000929	1.003852	1.000000	1.011828	1.000000	1.007604
64x64	1.000464	1.002035	0.999999	1.018134	1.000000	1.015315
	$\bar{\gamma}$	$\bar{\gamma}$	$\bar{\gamma}$	$\bar{\gamma}$	$\bar{\gamma}$	$\bar{\gamma}$
2x2	–	–	0.000000	0.001390	0.000000	0.000000
4x4	–	–	0.000000	0.002339	0.000000	0.000802
8x8	–	–	0.000000	0.004130	0.000000	0.001794
16x16	–	–	0.000000	0.007841	0.000000	0.003677
32x32	–	–	0.000000	0.015277	0.000000	0.007244
64x64	–	–	0.000000	0.030209	0.000000	0.013967

The results from Table 4 show that in pure bending cases with distributed moments all elements present similar and accurately converged results when a thin structure is considered. According to reference [20, p. 45], the line ad for the thin structure should be linear based on equivalence in the loading cases (Figure 5) but some discrepancies from the straight line can be found near the edges in the case of moderately thick plates. In the case of nodal forces at corners, both plate elements based on the absolute nodal coordinate formulation converge to

incorrect results, whereas SPACAR thin elements converge to correct results. Due to the fact that both of the loading cases should produce similar displacement fields for thin plates, it can be concluded that shear deformation is overly estimated in plate elements based on the absolute nodal coordinate formulation. This can also be seen in Table 5, where total rotation $\bar{\varphi}$ and shear angle $\bar{\gamma}$ are shown. In this example, locking is not observed. This indicates that similar error can be observed when using special material with $\nu=0$. According to the previous static and eigenfrequency analysis, the results are converged to incorrect results due to thickness locking. An interesting feature of the pure bending test is that it does not show inaccuracy due to thickness locking or slow convergence due to shear locking. On the other hand, according to eigenfrequency analysis, the second mode (saddle mode) indicates thickness locking (Tables 2 and 3). It can be noted that when using special material $\nu = 0$, all introduced plate elements lead to acceptable results in studied examples where shear deformation is not a dominating factor.

6 NUMERICAL TESTS FOR THICK PLATES

In the previous tests for thin plates, the SPACAR and fully parameterized elements were carefully considered. Based on the numerical results, it can be concluded that SPACAR plate elements perform well and fully parameterized plate elements perform acceptably, only for the case of pure bending. In this section, the behavior of the fully parameterized plate elements for thick plates will be examined. The SPACAR plate element is based on Kirchhoff theory, and for this reason, it can not be used for the analysis of thick plates.

6.1 PURE BENDING TEST

The numerical example introduced in this section is identical to the example shown in the previous section, with exception to the H/L relation which is increased to 0.2. The results show that in case of pure bending with distributed moments, elements give similar results for thin and thick plate examples. The displacement due to nodal forces at corners using thin plate SPACAR converges to the analytical solution for thick plates subject to pure bending. For shear deformable plate elements based on the absolute nodal coordinate formulation, line ad is not straight as can be seen in Fig. 7, where displacements due to nodal force loading of ANCF-P48lsa at line ad are shown. It is important to reiterate that the line should be straight [20].

6.2 THICK SIMPLY SUPPORTED PLATE UNDER UNIFORM STATIC LOAD

In this section, a thick plate is constrained with a simply supported condition and is loaded by the normal uniform force in the z -direction as shown in Fig. 8. The simply supported boundary condition is also depicted in the figure. In this example, the complete plate is modeled by using the same boundary conditions as in previous sections for simply supported plates.

The deflection at the middle of the plate for a fully parameterized ANCF-plate element is compared to the analytical result, based on the Reissner-Mindlin theory for a simply supported plate. This solution is presented in [22] as follows

$$w_0^M = w_0^K + \frac{M^K}{k_s G H} \quad (29)$$

where w_0^K is the Kirchhoff solution and M^K is the Marcus moment that is as

$$M^K = -D \nabla^2 w_0^K = \frac{1}{\pi^2} \sum_{m=1}^{\infty} \sum_{n=1}^{\infty} \frac{q_{mn}}{\frac{m^2}{L^2} + \frac{n^2}{W^2}} \sin \frac{m\pi X}{L} \sin \frac{n\pi Y}{W}. \quad (30)$$

Table 6: Normalized displacement at point a (Figure 5) of the square thick plate modeled by SPACAR, ANCF-P48 and ANCF-P48lsa elements. A relative plate thickness of $H/L = 0.2$ was used.

Mesh	SPACAR		ANCF-P48		ANCF-P48lsa	
	Moment	Forces	Moment	Forces	Moment	Forces
	\bar{w}	\bar{w}	\bar{w}	\bar{w}	\bar{w}	\bar{w}
2x2	1.014122	1.027241	1.000000	1.204565	1.000000	1.160000
4x4	1.003721	1.012120	1.000000	1.339463	1.000000	1.297473
8x8	1.000873	1.005163	1.000000	1.459176	1.000000	1.404434
16x16	1.000210	1.002256	1.000000	1.542509	1.000000	1.470083
32x32	1.000052	1.001033	1.000000	1.602122	1.000000	1.511021
64x64	1.000013	1.000491	1.000000	1.652936	1.000000	1.541885
	$\bar{\varphi}$	$\bar{\varphi}$	$\bar{\varphi}$	$\bar{\varphi}$	$\bar{\varphi}$	$\bar{\varphi}$
2x2	1.024127	1.050475	1.000000	1.065904	1.000000	1.000000
4x4	1.007862	1.025814	1.000000	1.109816	1.000000	1.063898
8x8	1.003778	1.013677	1.000000	1.171608	1.000000	1.133889
16x16	1.001864	1.007268	1.000000	1.215226	1.000000	1.179872
32x32	1.000929	1.003852	1.000000	1.237486	1.000000	1.205232
64x64	1.000464	1.002035	1.000000	1.247965	1.000000	1.220813

The Kirchhoff solution for the case of a simply supported plate, the deflection w_0^K obtained using the Navier solution is (see for example in [20]) as follows:

$$w_0^K = \frac{1}{\pi^4 D} \sum_{m=1}^{\infty} \sum_{n=1}^{\infty} \frac{q_{mn}}{\frac{m^2}{L^2} + \frac{n^2}{W^2}} \sin \frac{m\pi X}{L} \sin \frac{n\pi Y}{W} \quad (31)$$

where

$$\begin{aligned} q_{mn} &= \frac{4}{LW} \int_0^W \int_0^L q(X, Y) \sin \frac{m\pi X}{L} \sin \frac{n\pi Y}{W} dX dY \\ &= \frac{16q}{\pi^2 mn} \quad ; \text{ iff } m \text{ and } n \text{ odd} \end{aligned} \quad (32)$$

where $q(X, Y)$ is the uniformly distributed load, which is expressed as $q = -5 \cdot 10^6 H^3 \text{ N/m}^3$ for this example. The analytical solutions were computed using $m = n = 12$, which resulted in acceptable accuracy for normalized transverse displacement within four significant digits. In the case of a finite element solution, a uniformly distributed load is defined as a consistent load vector as follows:

$$F_{ext} = \int_{-1}^1 \int_{-1}^1 \int_{-1}^1 \mathbf{b}^T \mathbf{S} J d\xi d\eta d\zeta \quad (33)$$

where the body force is $\mathbf{b} = [0, q/H, 0]^T$. Other parameters are identical to previous sections. The normalized transverse displacements at the center of the plate are shown in tables 7-8.

In order to minimize the number of degrees of freedom, double symmetry for the plate under constant loading is used in the numerical example shown in Table 9. In double symmetry, the boundary conditions of sub domain are Ω boundary Γ_3 are as: $r_1 = 0$, $r_{3,x} = 0$ and $r_{1,z} = 0$ and for boundary as Γ_4 : $r_2 = 0$, $r_{2,z} = 0$ and $r_{3,y} = 0$. The boundaries Γ_1 and Γ_2 are simply

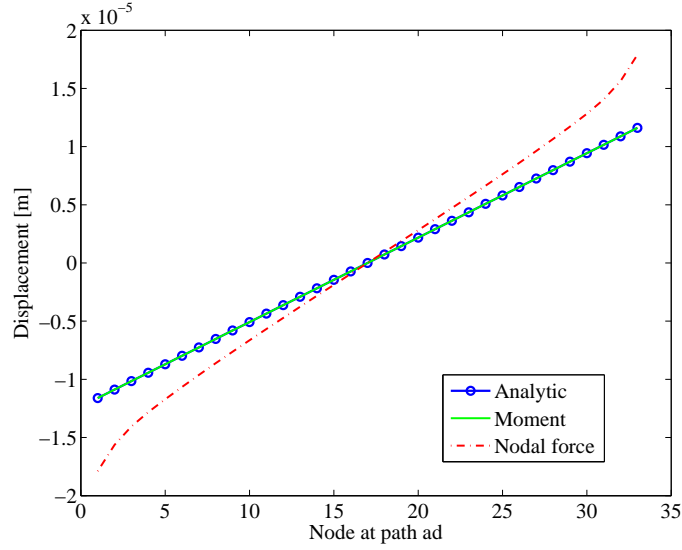


Figure 7: Displacements at asymptotic line ad , mesh 64×64 , ANCF-P48l_{sa}, $H/L = 0.2$.

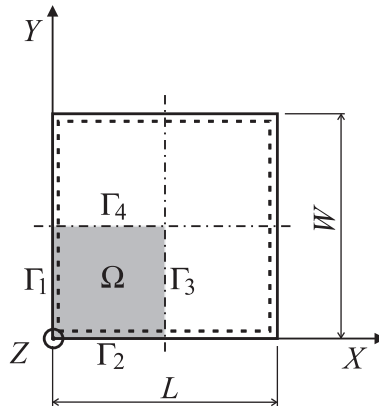


Figure 8: Simply supported plate, its sub domain Ω and the coordinate system.

supported, therefore r_1 and r_2 are fixed for boundary Γ_1 and r_2 and r_3 for Γ_2 . It can be seen in Table 9 that the displacements \bar{w} differ from displacements of the original problem (Table 8), where the converged displacements coincide to within three digits.

The relationship between Reissner-Mindlin and Kirchhoff theories (Eq. (29)) is valid only when Marcus moments are zero at the boundaries, which in practice, means the usage of "hard" simply supported conditions [22]. The results show that in the case of thin plates, the convergence of the plate element ANCF-P48 is slow; while the convergence of element ANCF-P48l_{sa} is more likely independent from the factor H/L . However, both plate elements converge to the same incorrect solution due to thickness locking. When Poisson effect is neglected, shear deformation is overestimated in case of thick plates.

Table 7: Normalized transverse displacement \bar{w} at center of the plate with ANCF-P48 loaded by a uniform loading.

Mesh	$H/L=0.001$	$H/L=0.01$	$H/L=0.1$	$H/L=0.2$
	\bar{w}	\bar{w}	\bar{w}	\bar{w}
2x2	0.0003151	0.02998	0.5333	0.6821
4x4	0.005940	0.3208	0.7210	0.8002
8x8	0.1013	0.6885	0.7742	0.8534
16x16	0.5428	0.7379	0.7938	0.8719
32x32	0.7259	0.7435	0.8011	0.8772
64x64	0.7417	0.7454	0.8032	0.8786

 Table 8: Normalized transverse displacement \bar{w} at center of the plate with ANCF-P48lsa loaded by a uniform loading.

Mesh	$H/L=0.001$	$H/L=0.01$	$H/L=0.1$	$H/L=0.2$
	\bar{w}	\bar{w}	\bar{w}	\bar{w}
2x2	0.8074	0.8077	0.8370	0.9107
4x4	0.7610	0.7614	0.79632	0.8768
8x8	0.7475	0.7481	0.7922	0.8731
16x16	0.7440	0.7449	0.7983	0.8768
32x32	0.7432	0.7448	0.8021	0.8784
64x64	0.7430	0.7456	0.8034	0.8789

7 RESULTS WHEN THICKNESS LOCKING IS REMOVED BY USING MODIFIED MATERIAL

Thickness locking can be avoided through use of higher order theories for the displacement field in the thickness direction or by modification of elastic coefficients. In case of fully parameterized ANCF plate element, it is not easy to determine the basis functions which can lead to a higher-than-linear displacement field in the thickness direction. However, in case of thin plates, the assumption $\sigma_{zz} = 0$ can be used to obtain modified in-plane elastic coefficients as follows:

$$D_{11} = \frac{E}{1 - \nu^2}; \quad D_{12} = D_{21} = \frac{\nu E}{1 - \nu^2} \quad (34)$$

 Table 9: Normalized transverse displacement \bar{w} at center of the plate with ANCF-P48lsa loaded by a uniform loading, the symmetry of the plate is used. $H/L = 0.2$

Mesh	ANCF-P48	ANCF-P48lsa
	\bar{w}	\bar{w}
2x2 (1x1)	0.6006	0.7353
4x4 (2x2)	0.7843	0.8625
8x8 (4x4)	0.8511	0.8711
16x16 (8x8)	0.8716	0.8766
32x32 (16x16)	0.8772	0.8784
64x64 (32x32)	0.8786	0.8789
128x128 (64x64)	0.8789	0.8790

However, it shall be noted that this is only suitable for thin plates and it does not produce a solution based on fully 3-D elasticity. In Table 10, the first ten eigenfrequencies of a free square plate for the ANCF-P48 element with modified material are shown. It can be concluded that the lowest eigenfrequencies correspond to the analytic results as well, but because of slow convergence due to shear locking, the converged eigenfrequencies are not reached.

Table 10: First ten dimensionless eigenfrequencies $\Omega = \omega/\omega_0$ of the free (ffff) square plate modeled by the ANCF-P48 with Poisson factor $\nu = 0.3$ for a number of mesh refinements. Thickness locking is neglected by using plane stress assumption. A relative plate thickness of $H/L = 0.01$ was used.

No.	1x1	2x2	4x4	8x8	16x16	32x32	64x64	Analytic
1	1.4383	1.4381	1.4234	1.3793	1.3655	1.3632	1.3618	1.3646
2	2.2739	2.2738	2.0380	1.9997	1.9882	1.9856	1.9850	1.9855
3	3.0985	3.0982	2.5636	2.4859	2.4646	2.4596	2.4584	2.4591
4	71.982	7.2347	5.5339	3.7007	3.5388	3.5230	3.5184	3.5261
5	71.982	7.2347	5.5339	3.7007	3.5388	3.5230	3.5184	3.5261
6	–	17.985	7.1124	6.3970	6.2335	6.1955	6.1862	6.1900
7	–	17.985	7.1124	6.3970	6.2335	6.1955	6.1862	6.1900
8	–	54.568	14.856	7.2267	6.5069	6.4460	6.4333	6.4528
9	–	72.207	16.632	7.7644	7.0798	7.0156	7.0017	7.0181
10	–	72.382	16.982	8.5799	7.8955	7.8216	7.8058	7.8191

Table 11: Average normalized transverse displacements \bar{w} and rotations $\bar{\varphi}$ at the loaded edge for a square cantilevered plate loaded by a distributed moment or a distributed transverse force at the free edge for a number of mesh refinements and $\nu=0.3$. Plate element ANCF-P48 is used and thickness locking is neglected by using plane stress assumption.

Mesh	Moment	Transverse force
1x1	1.0000	0.7501
2x2	1.0000	0.9376
4x4	1.0001	0.9846
8x8	1.0003	0.9964
16x16	1.0005	0.9996
32x32	1.0011	1.0009
64x64	1.0021	1.0020

It was expected that the slow convergence in case of transverse force occurs when plane stress assumption is used (Table 11). However, at this point, the convergence does not depend on the Poisson value because Poisson effect is neglected when using modified elastic coefficients. In case of the pure bending test, only minor differences were found when compared to the solution of 3-D elasticity. This also supports the assumption that the pure bending test which was used is free from thickness locking. However, the modified material is not a remedy for the slow convergence from in-plane shear locking.

8 DISCUSSION ABOUT DIFFERENT LOCKINGS FOR FULLY PARAMETERIZED PLATE ELEMENTS IN STUDIED BENCHMARKED PROBLEMS

The original fully parameterized plate element ANCF-P48 with 3-D elasticity suffers from several different lockings, which include shear, thickness and curvature lockings. In the fully parameterized plate element ANCF-P48lsa, shear and curvature lockings are avoided with an improved description of kinematics and by using low order interpolations for transverse shear deformations. However, according to the results, the thickness locking is still problematic for ANCF-P48lsa element.

Shear locking is occurs from the unbalance of the base functions [2]. This can be avoided by using the Assumed Natural Strain (ANS) technique, which is presented for shells in [2]. In papers [23, 15], the ANS technique is based on strains at the nodal values instead of strains at the Gaussian quadrature points. This is used because of the fact that parasitic strains are zero at the nodes [15]. To account for 3-D elasticity in the plate and shell formulations without thickness locking, the transverse normal strains have to be interpolated at least linearly over the thickness direction [24]. In contrast to other mentioned lockings, the error due to thickness locking does not decrease with mesh refinements in the in-plane coordinates. The plate element ANCF-P48 also suffers from curvature locking due to shrinking in the thickness direction. This locking effect is also mentioned to be problematic in other continuum plate/shell elements with coarse meshes and initially curved elements in [15]. In ANCF-P48lsa, curvature locking is avoided by using an improved description for kinematics.

When using the special case $\nu=0$ in 3-D elasticity, or using a modified material stiffness matrix, thickness locking can be avoided. Therefore, both plate elements converge to the analytic solution in most thin plate cases since coupling between bending and shear deformation is neglected. As a conclusion, in case of thin plates, the classical modified material which was used for 3-D plates can also be used to approximate a 3-D solution for thin plates modeled by fully parameterized plate elements. It shall be noted that the modified material stiffness matrix used in this study differs from the simplified material used in [11]. The same simplified material based on the diagonal material stiffness matrix $\mathbf{D} = \text{diag}(E, E, E, G, G, G)$ is also used for the continuum beam element [18], leading to similar results as obtained with beam theory. However, in case of plates/shells, such a simplified constitutive relation will obviously lead to an incorrect solution, which can be seen from the results in [11].

The results of benchmarked problems show that shear locking is strongly dependent on thickness whereas thickness locking is independent on thickness but strongly dependent on the Poisson effect. Due to thickness locking, the results differ by about 18 % from the analytical results, see Tables 1. However, for in-plane modes in the eigenfrequency analyses, thickness locking is difficult to recognize (Tables 2,3,10). The pure bending test that was used in the study is interesting because it can be used to question the accuracy of the shear deformation because it neither shows shear nor thickness locking (Table5). In the pure bending test, the same amount of error for shear angles occurs for the special case of $\nu = 0$ or when the modified material are used. In other words, when $\nu = 0$, both of the ANCF plate elements will pass all of the plate tests except for the saddle test and the simply supported plate test under uniform static load.

9 CONCLUSIONS

In this study, rectangular fully parameterized plate elements based on the absolute nodal coordinate formulation were compared in terms of numerical examples. Elements under investigation were a fully parameterized plate element and a fully parameterized plate element

with linearized transverse shear angles. The numerical examples demonstrate that the plate elements suffer from different lockings, however, thickness locking is dominant. The plate element with linearization of shear angles overcomes the slow convergence on account of shear locking and curvature locking. Due to thickness locking, both elements based on the absolute nodal coordinate formulation converged to the same incorrect solution in most of the numerical examples. The results also show that in case of thin and thick plates, the shear deformation was overestimated in both plate elements.

10 ACKNOWLEDGEMENTS

The authors would like to thank the Graduate School in Engineering Mechanics (Finland) for the support of Marko K. Matikainen.

REFERENCES

- [1] S. Ahmad, B. M. Irons, O. C. Zienkiewicz. Analysis of thick and thin shell structures by curved finite elements. *International Journal for Numerical Methods in Engineering*, **2**, 419–451, 1970.
- [2] E. N. Dvorkin, K-J. Bathe. A continuum mechanics based four-node shell element for general nonlinear analysis. *Engineering Computations*, **77**, 77–88, 1984.
- [3] N. Büchter, E. Ramm. 3D-extension of nonlinear shell equations based on the enhanced assumed strain concept. *Computational Methods in Applied Sciences*, 55–62, 1992.
- [4] R. G. Toscano, E. N. Dvorkin. A shell element for finite strain analysis: hyperelastic material models. *Engineering Computations*, **24**, 514–535, 2007.
- [5] A. A. Shabana. Definition of the Slopes and the Finite Element Absolute Nodal Coordinate Formulation. *Multibody System Dynamics*, **1**, 339–348, 1997.
- [6] J. Bonet, R. D. Wood. *Nonlinear continuum mechanics for finite element analysis*. Cambridge University Press, Cambridge, 2000.
- [7] L. G. Maqueda, A. A. Shabana. Poisson modes and general nonlinear constitutive models in the large displacement analysis of beams. *Multibody System Dynamics*, **18**, 375–596, 2007.
- [8] A. A. Shabana, Y. R. Yakoub. Three Dimensional Absolute Nodal Coordinate Formulation for Beam Elements: Theory. *Journal of Mechanical Design*, **123**, 606–613, 2001.
- [9] A. A. Shabana and A. P. Christensen. Three-dimensional absolute nodal co-ordinate formulation: plate problem. *International journal for numerical methods in engineering*, **40**, 2775–2790, 1997.
- [10] A. M. Mikkola, A. A. Shabana. A Non-Incremental Finite Element Procedure for the Analysis of Large Deformations of Plates and Shells in Mechanical System Applications. *Multibody System Dynamics*, **9**, 283–309, 2003.
- [11] A. M. Mikkola, M. K. Matikainen. Development of Elastic Forces for a Large Deformation Plate Element Based on the Absolute Nodal Coordinate Formulation. *Journal of Computational and Nonlinear Dynamics*, **1**, 103–108, 2006.

- [12] J. Gerstmayr, M. K. Matikainen, A. Mikkola. A geometrically exact beam element based on the absolute nodal coordinate formulation. *Multibody System Dynamics*, **20**, 359–384, 2008.
- [13] A.L. Schwab, J.P. Meijaard. Comparison of Three-Dimensional Flexible Beam Elements for Dynamic Analysis: Finite Element Method and Absolute Nodal Coordinate Formulation. *Proceedings of the ASME 2005 Int. Design engineering technical conferences & Computers and information in engineering conference, Long Beach, USA, September 24–28, 2005*.
- [14] J. Gerstmayr, A. A. Shabana. Efficient Integration of the Elastic Forces and Thin Three-Dimensional Beam Elements in the Absolute Nodal Coordinate Formulation. *Proceedings of the ECCOMAS Thematic Conference in Multibody Dynamics, Madrid, Spain, June 21–24, 2005*.
- [15] M. Bischoff, E. Ramm. Shear deformable shell elements for large strains and rotations. *International Journal for Numerical Methods in Engineering*, **40**, 4427–4449, 1997.
- [16] R. Hauptmann, S. Doll, N. Harnau, K. Schweizerhof. 'Solid-shell' elements with linear and quadratic shape functions at large deformations with nearly incompressible materials. *Computers and Structures*, **79**, 1671–1685, 2001.
- [17] A.L. Schwab, J. Gerstmayr, J.P. Meijaard. Comparison of Three-Dimensional Flexible Thin Plate Elements for Multibody Dynamic Analysis: Finite Element Formulation and Absolute Nodal Coordinate Formulation. *Proceedings of the ASME 2007 Int. Design engineering technical conferences & Computers and information in engineering conference, Las Vegas, USA, September 4–7, 2007*.
- [18] J. Rhim and S. W. Lee. A vectorial approach to computational modelling of beams undergoing finite rotations. *International Journal for Numerical Methods in Engineering*, **41**, 527–540, 1998.
- [19] G. M. Kulikov, S. V. Plotnikova. Equivalent single-layer and layer-wise shell theories and rigid-body motions-Part 1: Foundations. *International Journal for Numerical Methods in Engineering*, **12**, 275–283, 2005.
- [20] S. Timoshenko, S. Woinowsky-Krieger. *Theory of plates and shells*. McGraw-Hill, Tokyo, 1983.
- [21] O. N. Dmitrochenko, D. YU. Pogorelov. Generalization of plate finite elements for absolute nodal coordinate formulation. *Multibody System Dynamics*, **10**, 17–43, 2003.
- [22] C.M. Wang, J.N. Reddy, K.H.Lee. *Shear deformable beams and plates*. Elsevier, Amsterdam, 2000.
- [23] P. Betsch, F. Gruttmann, E. Stein. A 4-node finite shell element for the implementation of general hyperelastic 3D-elasticity at finite strains. *Computer Methods in Applied Mechanics and Engineering*, **130**, 57–79, 1996.
- [24] E. Carrera, S. Brischetto. Analysis of thickness locking in classical, refined and mixed multilayered plate theories. *Composite Structures*, **82**, 549–562, 2008.